Numerical Investigation of Autonomous Camber Morphing of a Helicopter Rotor Blade using Shape Memory Alloys

Etana Ferede
Research Scientist Rensselaer Polytechnic Institute, Troy, NY

Anargyros Karakalas
Post-Doctoral Researcher
Texas A&M University
College Station, Texas

Farhan Gandhi
Redfern Professor and MOVE Director
Rensselaer Polytechnic Institute, Troy, NY

Dimitris Lagoudas
Professor
Texas A&M University
College Station, Texas

ABSTRACT

Design and development of modern air vehicles seeks to produce airborne structures that are able to fly in a wide range of operational conditions with increased fuel efficiency and reduced environmental impact. To be able to operate efficiently throughout the operational envelop these structures need to be able to adapt their aerodynamic characteristics, a process achievable through the introduction of morphing regions. In this study, a numerical investigation of an autonomous camber morphing helicopter blade is presented considering Shape Memory Alloy materials able to undergo the Two-Way Shape Memory Effect. A series of designs and respective finite element analyses is employed to identify the effect of various parameters on various configurations that include the number of intermediate spars, the extend of the morphing section along the blade and the boundary condition between the pristine and the morphing portion. Overall, eliminating the need for pre-stress of the SMA component before being embedded in the host structure leads in significant reduction of the maximum strain and stress developed on the upper skin (passive component).

INTRODUCTION

Over the last couple of decades, the introduction of morphing in aerospace structures has been regarded as a highly effective means of achieving improved aerodynamic performance across diverse operating conditions (Refs. 1-5). One commonly considered form of morphing on both fixed- and rotary-wing aircraft has been wing or rotor blade camber change. Prior studies have considered several different camber actuation methods such as the use of piezoelectric actuators (Refs. 6-11), pneumatic actuators (Ref. 12), conventional servomotors (Ref. 13), and Shape Memory Alloys (SMA) (Refs. 14-18). Regardless of the tradeoffs associated with specific actuation methods, all morphing approaches require achieving some finite deformation in structures that are fundamentally rigid enough to withstand the aerodynamic loads, as well as centrifugal loads in the case of rotor blades. This, in turn, translates into significant actuation force or block stress and energy requirements.

In contrast, another approach to aircraft morphing is to exploit changes in operating state to realize structural shape change, without any dedicated actuation energy input. In rotary-wing aircraft, in particular, changes in rotor RPM, and the resultant changes in centrifugal forces acting on the blade, have been used in several studies to realize rotor span extension morphing (Refs. 15,16), chord extension morphing (Ref. 21), and rotor blade twist change (Refs. 22-26). Such an approach, where reconfiguration is achieved without the use of dedicated actuation energy input, is referred to as autonomous or passive morphing. A new autonomous morphing concept was proposed in Ref. 27 whereby an increase in helicopter rotor blade camber was realized with increase in ambient temperature. The camber change was achieved through the integration of temperature responsive SMA into the blade structure. Results from Ref. 27 showed that when the rotor was operating in hot and heavy load conditions (close to stall), the presence of the embedded SMA in the blade increased blade camber, the airfoil section's maximum lift coefficient, and the rotor lifting capability beyond that possible using a classical blade built with conventional material. However, the study also identified a number of design challenges such as the requirement of high pre-stress in the SMA and very high induced strains in the blade structure during morphing.

The current study seeks to advance and improve on the SMA-enabled autonomous camber morphing rotor blade concept developed in Ref. 27. Specific advancements include the use of trained SMA that present the Two-Way Shape Memory Effect (TWSME) that may significantly reduce or even eliminate high SMA pre-stress requirements and high strains in the blade at the undeployed/initial configuration. The study will also focus on details including a practical core structure to be used in the blade, specifics of attachment of the SMA to the blade and the core, and its effect on morphing performance.

The autonomous, camber morphing concept is based on a

Presented at the Vertical Flight Society's 77th Annual Forum & Technology Display, Virtual, May 10-14, 2021.

SC1095 airfoil and uses a NiTi (Ni 55.8 wt.%) SMA sheet actuator that replaces portion of the lower skin while at the Martensitic state. When the rotor is exposed at high ambient temperature the reverse transformation from Martensite to Austenite is initiated and the accompanied macroscopic deformation is leveraged to alter the camber of the airfoil shape. In this concept the integration of the SMA actuator in the pristine airfoil structure can be realized by adopting a wide range of configurations that include: (i) attachment of the SMA skin only to the blade spar and the trailing edge cap, but no attachment to the supporting corrugated inner structure, (ii) attachment of the SMA skin at one solid central corrugation, (iii) attachment of the SMA skin at two solid central corrugations and finally (iv) attachment of the SMA skin at every internal corrugation. Each configuration of the aforementioned setups is investigated in terms of the produced camber at certain ambient conditions, Martensitic Volume Fraction (MVF) of the SMA actuator as well as chordwise and spanwise strains at the deformed state.

SHAPE MEMORY ALLOYS

Materials that fall in the class of SMAs exhibit two distinctive characteristics, i.e., Shape Memory Effect (SME) and Pseudo-Elasticity (PE). Both phenomena are associated with their capability to produce and recover inelastic strains that are attributed to microscopic changes in their crystal structure. When a SMA is above a high temperature level denoted as A_f, the microstructure obtains the high symmetry phase of Austenite (A). As the material is cooled below a critical temperature denoted as M_f its crystal structure changes and twinned or self-accommodated Martensite (M^t) is formed. This transition does not induce any macroscopically observed change. Should the twinned Martensite be loaded above a critical stress level a detwinning process is initiated and an observable macroscopic strain is produced. This macroscopic strain reaches its maximum value when the detwinning process is completed and pure detwinned Martensite (M^d) is formed. Yet, removal of the mechanical load will not induce any macroscopic changes since the inelastic strain will remain. To recover this strain the material has to be heated above temperature levels that will initiate and complete the reverse transformation from Martensite to Austenite, denoted as A_s and A_f, respectively. The behavior exhibited during the thermo-mechanical cycle described is the so-called SME. This is also the phenomenon that can be leveraged to use these materials as actuation elements. The thermomechanical cycle described to induce the SME in SMA is presented in the Temperature-Stress-Strain space diagram provided in Fig. 1. In the schematic, the critical transformation thresholds for the initiation and completion of the reverse transformation (M➔A) are identified along with the critical stress thresholds for the initiation and completion of the detwinning process, i.e., σ_{ds} and σ_{df}, respectively. Finally, the inelastic, yet recoverable, deformation exhibited during the detwinning process is denoted in the schematic by ε^t.

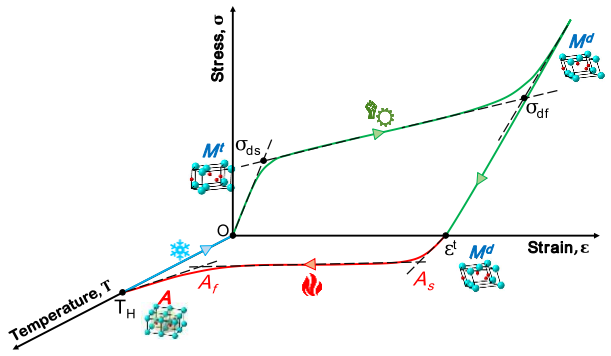

Fig. 1 SME in the temperature-stress-strain space.

In the work of Di Palma and Gandhi [27] the passive aluminum structure of the morphing airfoil section had to be designed to obtain a pre-flexed shape in order to provide a pre-strain and an associated pre-stress field to the SMA actuator that could result in maintaining a detwinned Martensitic state and render it possible to induce the reverse transformation. This process becomes quite complicated in terms of designing effectively such a structure, since the stiffness of the selected core, the magnitude of the initially built-in reflex and the thickness of the SMA component as well as its pre-strain must be determined in order to reach a configuration near the one of the pristine/reference blade geometry. This whole process could be less cumbersome if the SMA component had the capability to present a TWSME and be able to recover and produce transformation strain under zero or small stress levels. Thus, in this work a trained NiTi (Ni 55.8 wt.%) SMA is considered.

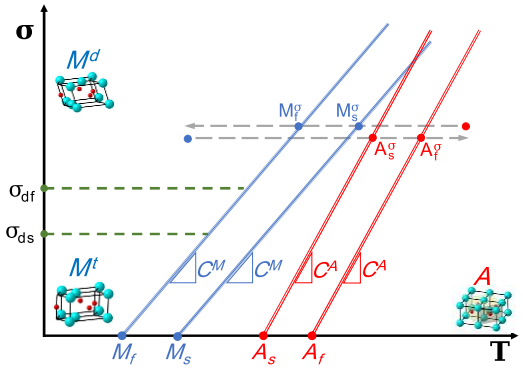

Fig. 2 SMA phase diagram.

During a training process the material is subjected to cyclic thermal loading under a constant stress level, often higher than the maximum anticipated one when under operational conditions. Cycling between a fully Austenitic and a fully detwinned Martensitic state generates internal stresses in the microstructure that affect the exhibited transformation behavior. A trained SMA material is able to produce considerable amount of transformation strain when transitioning from the parent phase of Austenite to the product phase of Martensite at small or even zero stress levels. In such a case, the internal stresses introduced at micro-structural level allow for the alignment of Martensitic variants at preferable directions as well as maintaining the detwninned

state. Although pre-straining and, consequently, pre-stressing of the SMA material might prove beneficial, since it increases the maximum available transformation strain, it also affects the critical transformation temperature thresholds. These temperature limits increase with higher stress levels, which in turn means that in order to initiate a transformation process higher temperature levels have to be achieved, as shown in the SMA phase diagram presented in Fig. 2. Consequently, SMAs capable of recovering transformation strains at zero load are more favorable for the design of morphing structures since they require less complex design considerations.

SMA Constitutive Model

To predict the non-linear constitutive behavior of the NiTi (Ni 55.8 wt.%) SMA material considered in this study, the baseline constitutive model of Lagoudas et al. [28] as extended by Hartl et al. [29] and Karakalas et al. [30] is adopted and implemented in the Abaqus FE software through a specialty user material (UMAT) subroutine. The model is able to account for TWSME by considering a maximum transformation function, called H^{cur} that is postulated as follows:

$$H^{cur}(\sigma) = H_{sat}\left(1 - e^{-k_t \bar{\sigma}^{eff}}\right) \qquad (1)$$

where H_{sat} is the saturation transformation strain, k_t is an experimentally calibrated parameter that controls the rate that maximum transformation strain evolves with the applied stress level, while $\bar{\sigma}^{eff}$ is the effective Von Mises stress. This stress is calculated based on the well-known Von Mises criterion, yet the components of the stress tensor considered are based on Eq. (2), where $\boldsymbol{\beta}$ is a second order tensor named as back-stress. The values for the back-stress are calibrated based on experimental data.

$$\boldsymbol{\sigma}^{eff} = \boldsymbol{\sigma} + \boldsymbol{\beta} \qquad (2)$$

The back-stress tensor accounts for the internal stresses generated in the microstructure during training process. The developed stress fields lead to retainment of detwinned Martensitic variants, thus upon heating the material is able to transform directly between the detwinned Martensitic and Austenitic state, i.e., recover an amount of transformation strain available. Furthermore, as externally applied stress increases the value of the available transformation strain increases as well (as per Eq. (2)) till reaching the saturation strain level (H_{sat}). To this end, it becomes apparent that high back-stress values would result in higher available transformation strain and, consequently, higher camber adaptation upon thermal activation of the actuator. The salient material properties of the SMA selected this study are summarized in Table 1.

CONCEPT DESCRIPTION AND ANALYSIS

For the purposes of the work presented herein, a prismatic derivative of the UH-60A Black Hawk helicopter blade (with constant chord of 0.5 m and zero twist) with a SC1095 airfoil along the entire span has been selected. For initial analysis, a morphing airfoil section (strip) is considered and assumed to have a spanwise length of 10% of the chord. A rigid leading-edge spar extends from the leading edge of the blade to 25% of the chord, while the conformable region occupies the area between 25 and 80% of the chord. Finally, the trailing edge consists of a relatively stiff aluminum cap. The conformable region between the leading and the trailing edge consists of: (i) 0.5%c (chord) thick upper skin comprised of aluminum sheet with Young's modulus of 72 GPa and Poisson's ratio of 0.3, allowing the upper skin to remain stiff under nominal loads yet being able to elastically deform when the airfoil is morphed; (ii) a intermediate spar, comprised of the same material as the upper skin, is placed between the conformable upper and lower skin; and (iii) a smart lower skin manufactured from an SMA sheet 0.5%c thick. When ambient temperature exceeds a critical limit, the reverse transformation from Martensite to Austenite will initiate resulting in the recovery of the available transformation strain. The camber of the airfoil increases as the lower skin contracts changing the aerodynamic characteristics of the airfoil. The autonomous morphing concept described in this paragraph is schematically presented in Fig.3.

Table 1. SMA Material Properties and Parameters

Symbol	Value	Units
E^A	66.2	GPa
E^M	25.6	GPa
ν	0.33	-
C^A	9.02	MPa/K
C^M	8.34	MPa/K
M_f	283.0	K
M_s	311.0	K
A_s	313.0	K
A_f	366.0	K
H^{sat}	0.059	-
k_t	$2.25\ 10^{-8}$	1/Pa
β_{1D}	200.0	MPa

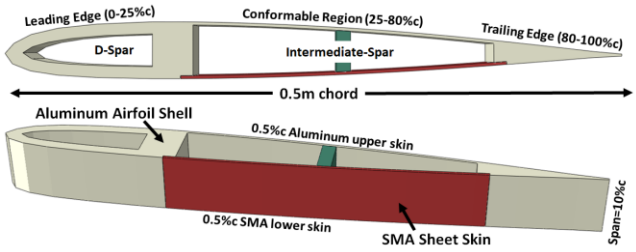

Fig.3 Schematic representation of the autonomous morphing concept

The structural analysis of the morphing section is conducted using ABAQUS 6.13 Finite Element Analysis software. The D-spar region of the airfoil section is modelled using 800, 8 node brick elements with reduced integration and enhanced hourglass control (C3D8R). The conformable upper airfoil skin is modelled using, respectively, 40, 2, 10 C3D8R elements along the chord, thickness, and span

direction (800 elements in total). The trailing edge region is modelled using 280 C3D8R elements. The SMA skin is modelled using, respectively, 72, 2, and 10 C3D8R elements along the chord, thickness, and span direction (1440 elements in total). A sample of the Finite Element (FE) mesh is shown in Fig. 4.

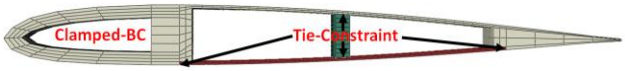

Fig. 4 Sample of finite element mesh.

The D-Spar, upper skin, and the trailing edge are modelled as one part, with clamped boundary condition imposed on the D-Spar along the entire span. Furthermore, a 'Tie-constraint' (merging of all applicable degrees of freedom between the connected cells) is used to attach the intermediate spar (green elements in Fig. 4) to the conformable upper skin and the lower skin. Additionally, the lower (SMA) skin is attached to the D-Spar and the trailing edge using 'Tie-constraint'. The type of FE analysis selected was "static-general" since the present study focuses on a conceptual analysis and time related phenomena, such as heat fluxes as well as dynamic response of the simulated structure are considered out of the scope. Finally, due to the non-infinitesimal rotations presented upon activation of the SMA active component the effect of geometric non-linearities is properly accounted for. Numerical investigations entailing SMA actuators have proved that omitting the effect of large rotations on the calculated constitutive response might result in erroneous predictions both in terms of the internal state as well as the exhibited stress and strain levels [31].

The aerodynamic pressure loads are obtained from XFOIL analysis of SC1095 airfoil, both for the baseline and deformed shape. The details on how the aerodynamic pressure loads are obtained can be found in the work of Di Palma and Gandhi [22]. XFOIL evaluation of the pressure distributions is carried out for Mach number 0.55 and at 5° of angle of attack, with Fig. 5 showing the pressure variation over the upper and lower surface of the airfoil, both for the baseline and cambered airfoil geometry. Finally, a factor of safety of 2 is applied to the aerodynamic pressure load during the structural analysis in ABAQUS.

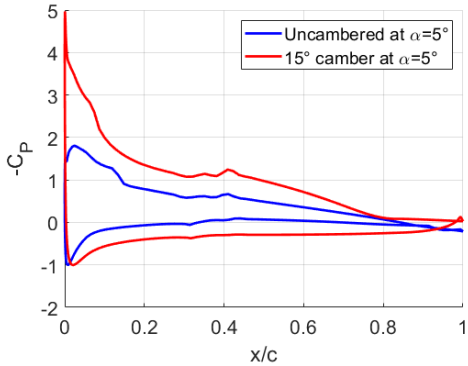

Fig.5 Chordwise CP comparison between baseline SC1095 and 15° cambered derivative at $\alpha = 5^{\circ}$ [22].

RESULTS

Camber Morphing over Airfoil Section

An initial set of analyses is carried out to determine the minimum number of intermediate spars (see Fig. 3) that result in maximum camber deformation of the airfoil section for a specified change in ambient temperature while providing enough support to the SMA skin to prevent local out-of-plane deformation of the lower skin under effect of aerodynamic pressure fields. The out-of-plane deformation refers to the localized deformation/warping of the SMA skin resulting in non-smooth lower surface of the airfoil. To this end several FE analyses are performed for an airfoil section with increasing number of vertical spars. Figures 6 to 9 show the Martensite-to-Austenite transformation and the resulting camber deformation under applied change in ambient temperature (45°F to 170°F) without considering aerodynamic pressure load.

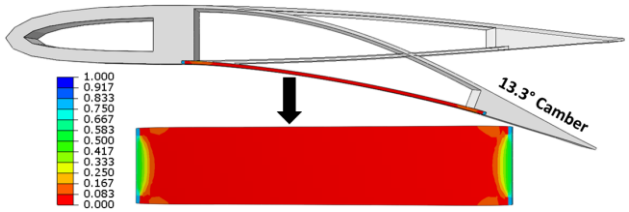

Fig. 6 Unsupported lower (SMA) skin configuration; cambered airfoil section and the associated MVF distribution of the SMA skin.

In Fig. 6, when the SMA on the lower surface is attached only to the spar and the trailing-edge cap, temperature increase produces Martensite to Austenite phase change over the majority of the SMA (except the regions where it is bonded to the blade) and a large change in camber (13.3°) is observed.

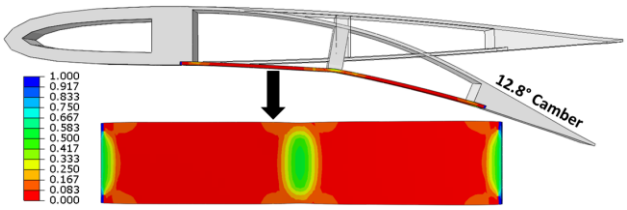

Fig. 7 Lower (SMA) skin supported with one vertical spar; cambered airfoil section and the associated MVF distribution of the SMA skin.

In Fig. 7, in addition to the spar and the trailing-edge cap, the SMA is attached to one intermediate spar. As with the end attachments, the SMA is not allowed undergo phase transformation at the attachment to the intermediate spar upon heating. However, there is sufficient region of SMA skin that is free to transform from Martensite to Austenite and recover the available transformation strain. Thus, no appreciable reduction in camber is observed (relative to Fig. 6).

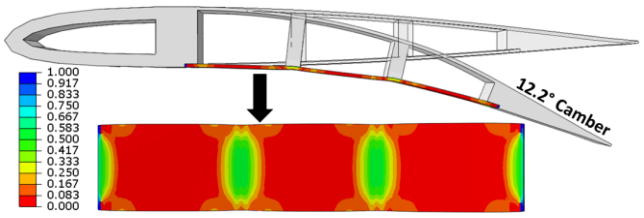

Fig. 8 Lower (SMA) skin supported with two vertical spars; cambered airfoil section and the associated MVF distribution of the SMA skin.

In Fig. 9, the SMA is now attached to two intermediate spars. No phase change occurs along the attachments upon heating, yet the camber achieved due to Martensite to Austenite phase change in the unbonded SMA results in a limited reduction in achievable camber change that is only 1.1° compared to the maximum camber deformation shown in Fig. 6. This can partially be attributed to large portion of the SMA region that is not constrained by the spars thus capable of undergoing full Martensite-to-Austenite transformation.

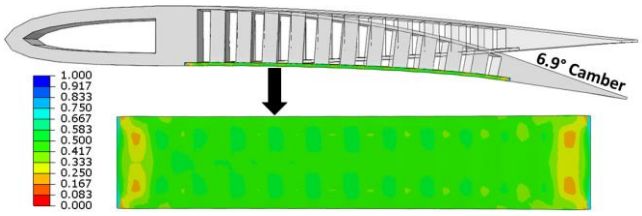

Fig. 9 Lower (SMA) skin supported with semi-continuous vertical spars; cambered airfoil section and the associated MVF distribution of the SMA skin.

Finally, in Fig. 9, the SMA is attached to semi-continuous intermediate spars located between the D-Spar and the trailing edge. This significantly reduces the active SMA volume available and a much smaller camber deformation is observed, see Fig. 10 for the relation between the number of supporting spars and the resulting camber deformation. The small deformation also correlates to a smaller volume change from Martensite to Austenite. In Fig. 9, roughly 50% Martensite-to-Austenite transformation is realized across most of the SMA sheet in contrast to fully achieved transformation across the majority of the SMA sheet in Figs. 6-8. Two intermediate spars for supporting the SMA sheet (see Fig 8) is the best compromise between achieving large camber deformation while providing sufficient support to the SMA skin in preventing local deformation of the lower skin under aerodynamic load.

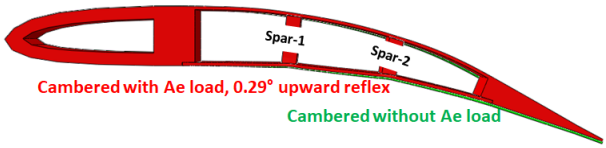

Fig. 11 Global deformation of the cambered airfoil section under aerodynamic load.

Additional analysis is carried out including aerodynamic pressure load (see the red curve in Fig. 5 for the pressure distribution over the airfoil) to verify that the configuration where the SMA skin is supported by two intermediate spars possesses sufficient bending stiffness to resist local deformation under aerodynamic pressure load. Figure 11 shows the global deformation of the airfoil section after heating the SMA skin to 170°F and applying aerodynamic load. A relative upward reflex camber of 0.29° is observed when aerodynamic load is applied.

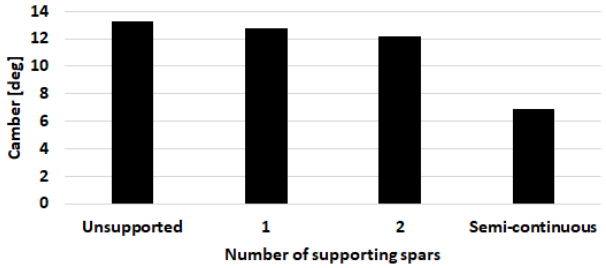

Fig. 10 Camber versus number of supporting spars for morphing airfoil section.

Furthermore, Fig. 12 shows the downward displacement of the SMA skin along the (non-dimensional) chordwise coordinate of the SMA skin. The black curve represents the downward deflection of the SMA due to change in ambient temperature only, while the red curve shows the SMA deflection including aerodynamic load. Comparing the two deformation curves of the SMA skin in Fig. 12 shows that, in conjunction with the two intermediate spars, the SMA skin possesses sufficient bending stiffness to resist local out-of-plane deformation under applied aerodynamic load.

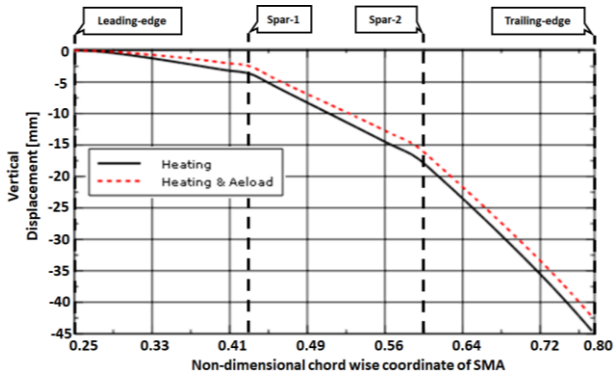

Fig. 12 Deformation of the SMA skin due to change in ambient temperature and applied aerodynamic load.

Figure 13 shows magnitude of the camber deformation as a function of the ambient temperature, both for the heating and cooling phase. The camber-temperature hysteresis shown in Fig. 13 is for the airfoil section with two intermediate spars (see Fig. 8). During the heating cycle, the Martensite-to-Austenite phase transformation does not start until the ambient temperature reaches 95°F. Afterwards, the phase transformation starts and finishes when the temperature reaches 170°F, resulting in maximum camber deformation of 12.2°. A significant gradient in high temperature would induce a less significant reduction in achievable camber deformation, i.e., if the ambient temperature is 135°F instead of 170°F, the camber loss would be limited to 2.2°.

Figure 14 shows the corresponding chordwise strain in the SMA skin at the end of the heating (HOT) and cooling (COLD) cycle. A maximum chordwise strain of 6.3% (in tension) is observed at the end of the heating cycle. The maximum strain is over the unconstrained region of the skin, where the SMA material is free to fully transform from Martensite to Austenite. Parts of the SMA strip attached to the airfoil section show reduced chordwise strain, which is the result of reduced phase transformation. There is a slight residual chordwise strain at the end of the cooling cycle, with a maximum strain of 0.6% (compression) in the unconstrained region of the SMA skin.

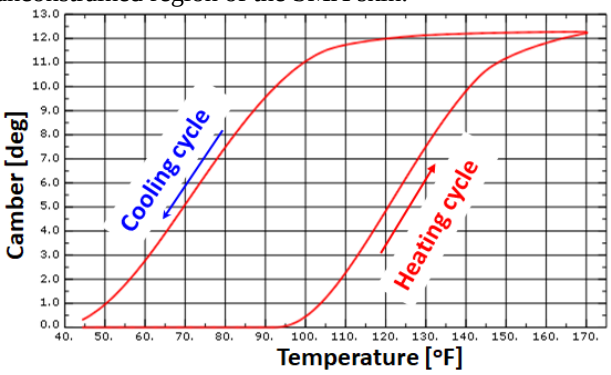

Fig. 13 Camber versus temperature for an airfoil section with two intermediate spars.

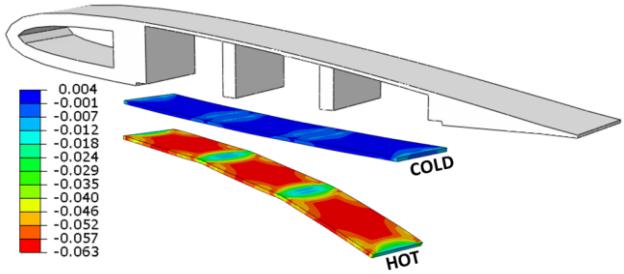

Fig. 14 Chordwise strain in the SMA for an airfoil section with two intermediate spars. Hot indicates at the end of heating cycle and Cold indicates at the end of cooling cycle.

Figure 15 shows the corresponding maximum in-plane principal strain along the (conformable) upper skin and the two intermediate spars. Large strains are observed in the cambered state of the airfoil section. These large strains are located at the connection points between the intermediate spars and the SMA skin, with the absolute strain reaching up to 0.6%. The large strains at the connection region (between the intermediate spars and SMA skin) is partially due to large spanwise strain developed in the SMA material during the phase transformation. Furthermore, only the upper surface of the SMA skin is connected to the intermediate spars resulting in non-uniform strain across the thickness of the SMA skin (solely in regions of SMA connected to the spars). Furthermore, a small strain in the upper skin is observed (around 0.1%), just aft of the intermediate spar closest to the trailing edge.

Finally, Fig. 16 shows the corresponding von Mises stress along the upper skin and the two spars that support the SMA skin. Similar to the strain state shown in Fig. 15, large stress is observed during the cambered state of the airfoil section. Large stress is developed at the connection points between the spars and the SMA skin. This large stress gradient at the connection points is partially due to the inability of the SMA skin to expand in the spanwise direction (region of the SMA skin connected to the spars) causing stress concentration at the connection points. Furthermore, there is through the thickness variation of stress in regions of the SMA skin attached to the intermediate spars, causing stress concentration at the connection points (between SMA skin and intermediate spars). The highest Mises stress along the (conformable) upper skin is aft the intermediate spar located near the trailing edge.

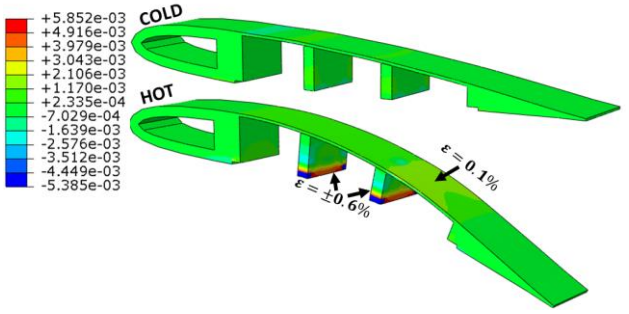

Fig. 15 Maximum in-plane principal strain over the upper (conformable) skin and the two intermediate spars. Hot indicates at the end of heating cycle and Cold indicates at the end of cooling cycle.

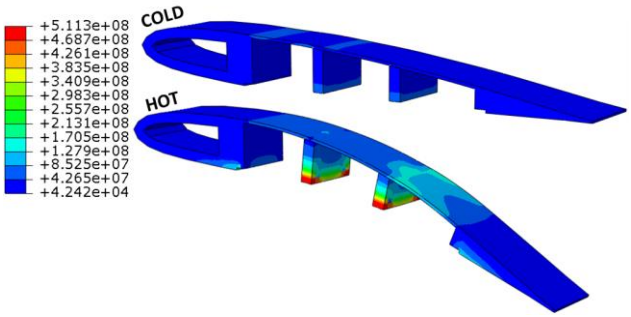

Fig. 16 Von Mises stress (Pa) over the upper (conformable) skin and the two intermediate spars. Hot indicates at the end of heating cycle and Cold indicates at the end of cooling cycle.

Camber Morphing Over Inboard 50% Span, Slit junction

The first set of full span analysis is carried out for morphing blade section that extends 50% inboard of the prismatic derivative of the UH-60A Black Hawk helicopter blade. A slit boundary is imposed between the morphing and non-morphing section. Figure 17 shows the spanwise morphing blade section in baseline and cambered state. An SMA sheet (0.75c wide by 0.5Span long by 0.05%c thick) is attached to the lower surface of the morphing blade section.

The SMA skin is heated by raising the ambient temperature from 45°F to 170°F with the resulting deformation of the SMA sheet shown in Fig. 18. Looking at Fig. 18, the SMA experiences compressive stress in spanwise direction during the heating cycle resulting in the buckling-like behavior

of the SMA sheet. Since the material is considered initially at the detwinned Martensitic state, this means that there an amount of transformation strain developed along the chord wise direction. However, transformation strain is considered to be isochoric meaning that if a strain is produced along a direction half this amount of strain will be also present in the perpendicular directions, so that the overall volume is retained. Thus, once thermal activation of the SMA material induces the recovery of the transformation strain along the chord-wise direction, there will be strain generated towards the span-wise and through-the-thickness directions. In order to bypass the buckling-like behavior of the SMA sheet, a series of SMA strips are attached to the lower surface of the blade section then overlaid by a thin continuous sheet of elastomer skin.

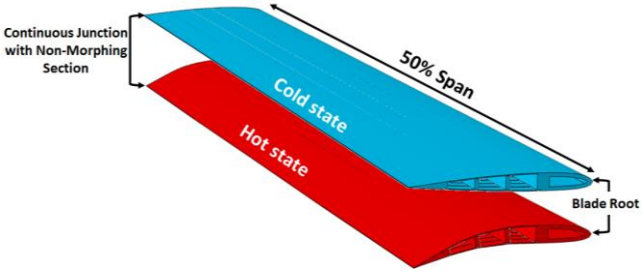

Fig. 17 Low-and high-temperature states with a slit between morphing and non-morphing sections.

The elastomer skin serves to provide a smooth outer surface to retain the aerodynamic profile of the blade section. However, the thin elastomeric skin does not provide structural support and thus is omitted from the present (structural) analysis. The SMA strips are attached along the span of the blade section with 2 mm gap between the SMA sheets (See Fig. 19). The gap ensures that the SMA strips do not overlap during heating cycle, since they expand in spanwise direction as the material transitions from Martensitic to Austenitic phase.

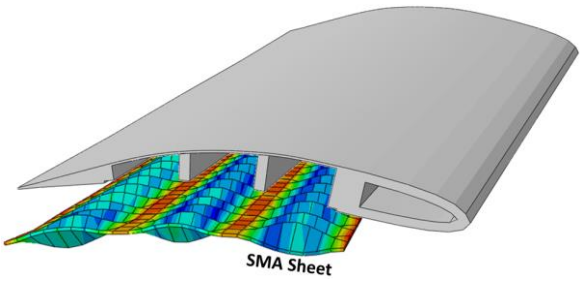

Fig. 18 Buckling of the SMA sheet.

The width of the SMA strips is determined iteratively by performing phase transformation analysis for successively narrower strips until the blade section deforms without the SMA strips presenting buckling-like behavior. An SMA strip, 0.1c wide, is narrow enough to prevent the unwanted deformation of the material while providing the required force to deform the blade section to a sufficiently large camber angle.

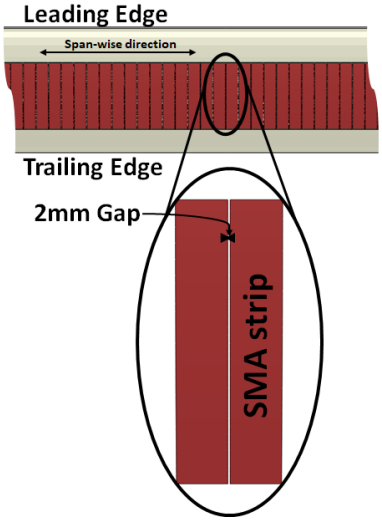

Fig. 19 Span-wise attachment of SMA strips to the blade section.

Once the desired width of the SMA strips is obtained, structural analysis of the morphing blade section is carried out including the presence of a centrifugal load. The centrifugal load is calculated for an angular velocity of 27 rad/s, which represents the rotor speed of the UH-60A Black Hawk helicopter in hover. Figure 20 shows the magnitude of the camber deformation versus the ambient temperature for the blade section with slit boundary condition. The camber vs temperature trend is similar to the airfoil section (see Fig. 13). However, in the case of the blade section (Fig. 20), the maximum camber of 11.5° is slightly less than that of the airfoil section. The most probable reason for the slight reduction in camber is due to the gaps between the SMA strips on the blade section (see Fig. 19). While these gaps allow the strips to expand without overlapping, the total amount of SMA material is slightly reduced thus decreasing the amount of force the SMA skin generates, for the same increase in ambient temperature, to deform the blade section.

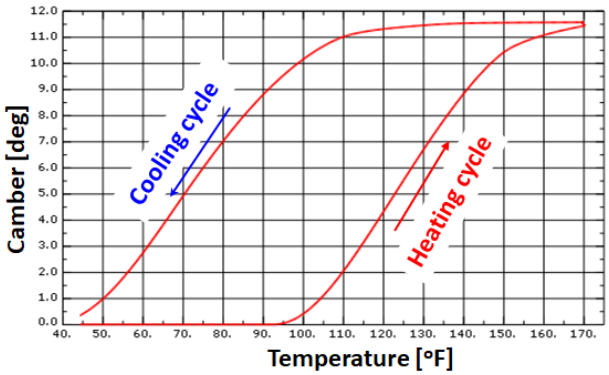

Fig. 20 Camber versus temperature for the blade section with slit boundary condition between the morphing and non-morphing parts of the blade.

Figure 21 shows the Martensitic volume fraction of the SMA strips along the lower blade surface, both for Hot (cambered) and Cold (uncambered) state. At the highest temperature (Hot-state), full transformation is achieved in

the unconstrained region of the SMA skin, while the constrained region (parts of the SMA strips connected to the D-Spar, supporting spars, and the trailing edge) achieve 47% transformation to the Austenite phase (mirroring the results for the airfoil section in Fig. 6). Furthermore, a full recovery to the Martensitic state is achieved at the end of the cooling cycle.

Figure 22 shows chordwise strain in the SMA skin. At maximum deformed state of the blade section (Hot-state), a spanwise constant strain of 6% is observed over the unconstraint region of the SMA strips. Furthermore, a small compressive strain of 0.2% is observed at the end of the cooling cycle (Cold-state).

Figure 20 presents the corresponding maximum in-plane strain along the upper blade surface and the supporting two spars. Large strains are observed in the Hot-State where the blade section undergoes a maximum downward camber deformation of 11.5º. The highest strain in the upper surface is 0.17% (constant in spanwise direction), located between the trailing edge section and the closest supporting spar.

Finally, Fig 24 shows the von Mises stress along the upper surface of the blade section and the supporting spars. A maximum stress of 124MPa is observed over the aft region of the conformable upper skin of the blade section, which is far less than the yield strength of Aluminum. Similar to Fig. 23, the maximum stress is constant along the blade span. The blade section is relatively stress free in the cold-state, with the residual stress caused mostly by the centrifugal load.

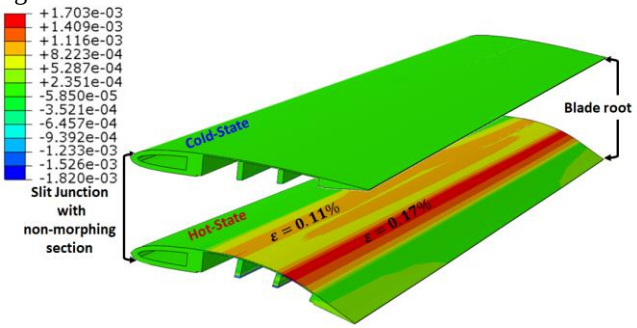

Fig. 23 Maximum in-plane strain in the upper (conformable) skin and supporting spars; with slit boundary condition between the morphing and non-morphing parts of the blade.

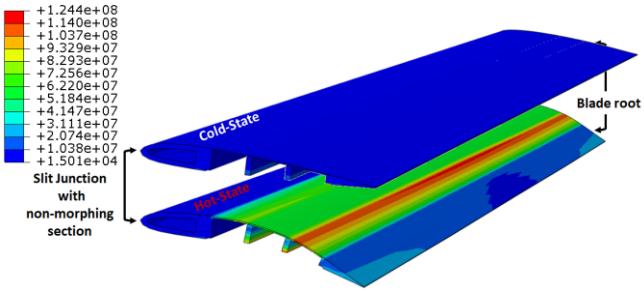

Fig. 24 Von Mises stress (Pa) in the upper (conformable) skin and supporting spars; with slit boundary condition between the morphing and non-morphing parts of the blade.

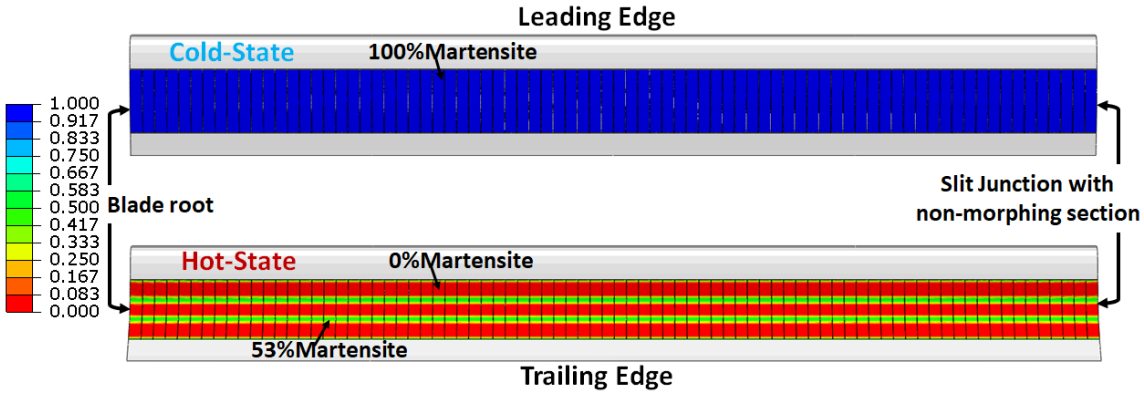

Fig. 21 Martensite volume fraction in the SMA strips along the lower blade surface with slit boundary condition between the morphing and non-morphing parts of the blade.

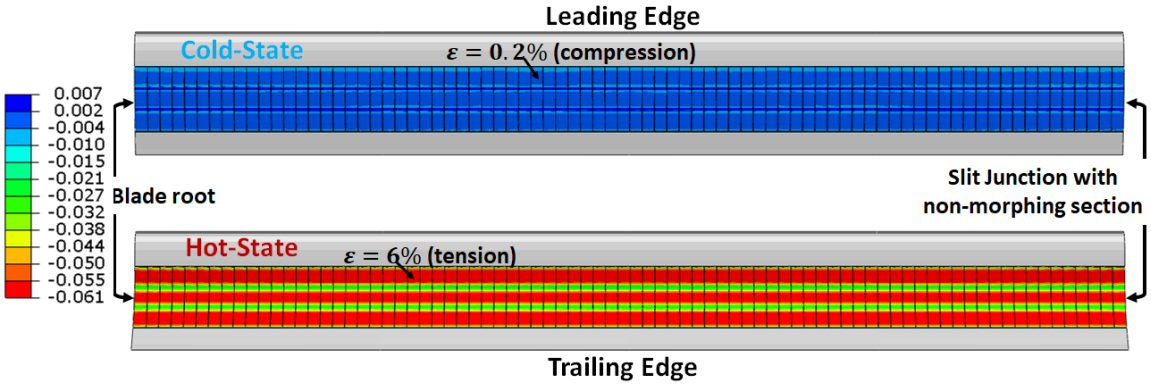

Fig. 22 Chordwise strain in the SMA strips along the lower blade surface with slit boundary condition between the morphing and non-morphing parts of the blade.

Camber Morphing Over Inboard 50% Span, Continuous junction

The next analysis considers another configuration of the morphing blade section, where a continuous boundary condition is imposed with the non-morphing section of the blade (seamless integration). Figure 25 shows a representation of baseline and cambered configuration of the blade section that accounts for seamless integration with the non-morphing section.

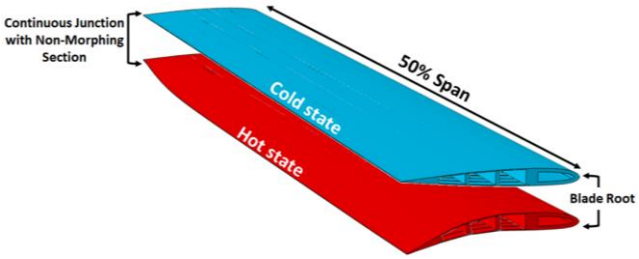

Fig. 25 Low-and high-temperature states for seamlessly integrated morphing section.

The remaining set of results are from an analysis case where the seamlessly integrated morphing section is run through the heating and cooling cycle by increasing the ambient temperature from 45°F (Cold) to 170°F (Hot) while considering centrifugal load. The centrifugal load is evaluated at the angular velocity of 27rad/s (same as in the previous analysis case). The (blade) root camber vs. the temperature trend is similar to that of the blade section with slit boundary condition (see Fig. 20). Camber variation along the (non-dimensional) spanwise coordinate is presented in Fig. 26. The red and blue curve show, respectively, the spanwise camber deformation at the end of the heating and cooling cycle. Large gradient in camber deformation is observed close to the junction with non-morphing section. The zero camber at the junction increases sharply and reaches the maximum camber of 11.5° at 38% span. A uniformly un-cambered state is achieved at the end of the heating cycle (see blue curve in Fig. 26).

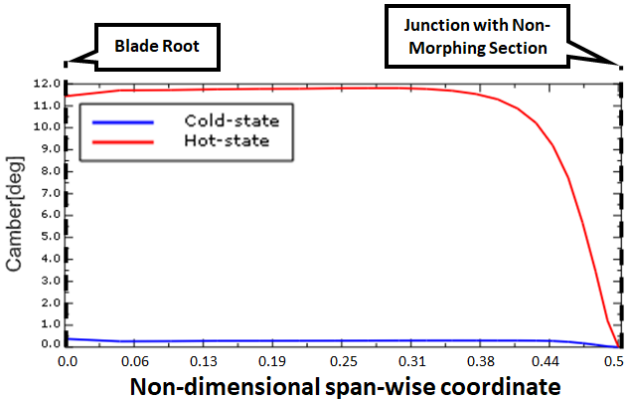

Fig. 26 Inboard camber distribution for seamlessly integrated morphing blade section.

The corresponding Martensitic volume fraction in the SMA strips is shown in Fig. 27. It is evident from Fig. 27 that, at the end of the heating cycle, a complete transformation (Martensite-to-Austenite) is achieved over most of the SMA region that is not attached to the supporting spars. This results in the maximum achievable camber (for a given set of SMA properties) over most of the morphing blade section (0-38% span in Fig. 26). However, almost no phase transformation occurs close to the junction with the non-morphing section of the blade since the boundary condition imposed at the junction prevents the local SMA strips to undergo phase transformation. A full recovery of Martensite state is achieved at the end of the cooling cycle (see Cold-state in Fig. 27) resulting in the full recovery of the baseline blade configuration.

Figure 28 presents the corresponding chordwise strain of the SMA strips, at the end of the heating (Hot-state) and cooling (Cold-state) cycle. Similar trend is observed between the chordwise strain and the Martensite volume fraction where a uniform tensile strain of 6% is achieved over most of the SMA strips (between 0-38% span). The SMA strips close to the junction with the non-morphing blade section experience compressive strain (up to 1.6%) due to the imposed boundary condition at the continuous junction region. A small compressive strain (up to 0.3%) is observed in the baseline configuration (Cold-state).

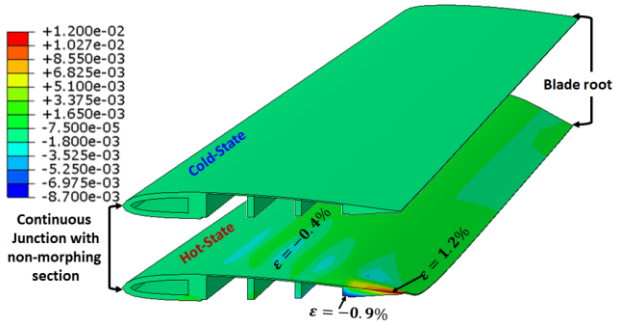

Fig. 29 Maximum in-plane strain in the upper (conformable) skin and supporting spars for seamlessly integrated morphing section.

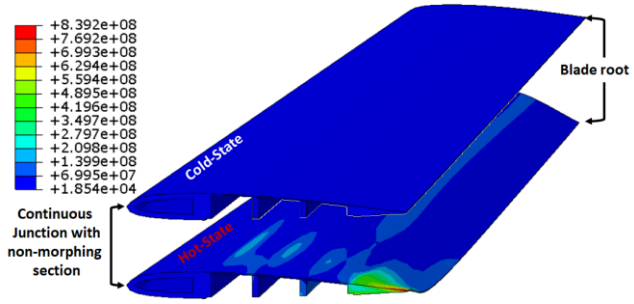

Fig. 30 Von Mises stress (Pa) in the upper (conformable) skin and supporting spars for seamlessly integrated morphing section.

Figure 29 shows the maximum in-plane strain along the upper surface and supporting spars of the morphing blade section. Large strain values (-0.9% to +1.2%) are observed around the trailing edge of the morphing blade section, near

the junction with the non-morphing part of the blade. These high strains are induced by the large camber gradient close to the junction with the non-morphing section (see Fig. 26). Several options are available to alleviate the large strains, such as: (i) modify the properties of the SMA strips located near the junction through proper heat treatment or other post-processing techniques such that the strips deform less for the same variation in ambient temperature; (ii) increase the gap between the SMA strips near the junction which results in reduced force applied by the SMA strips to the morphing section; and (iii) tailor the cross-sectional stiffness of the morphing section near the junction to achieve smaller camber gradient near the junction to the non-morphing section.

Figure 30 shows the corresponding von Mises stress along the upper skin of the morphing section and the supporting spars. Similar to Fig. 29, large stress concentration is observed around trailing edge section that is close to the junction with the non-morphing part of the blade. Again, these stress concentrations are the result of the large camber gradient observed near the junction, as shown in Fig. 26 and can be alleviated by proper re-design of the morphing section components and the applied connections.

Finally, it should be noted that unlike in the work of Di Palma and Gandhi [27], removing the need to provide a pre-strain to the baseline configuration has significantly reduced the maximum strain and stress in the upper (conformable) skin and the rest of the morphing blade section.

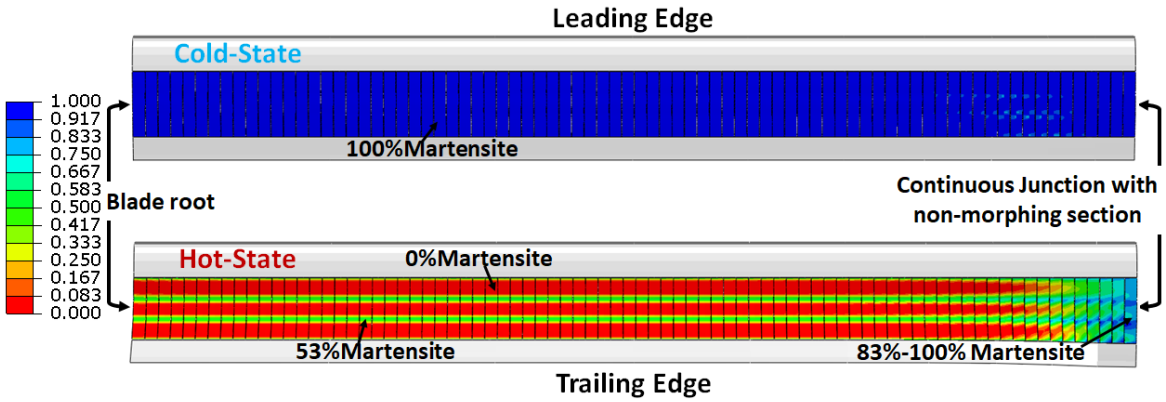

Fig. 27 Martensite volume fraction in the SMA strips along the lower blade surface for seamlessly integrated morphing section.

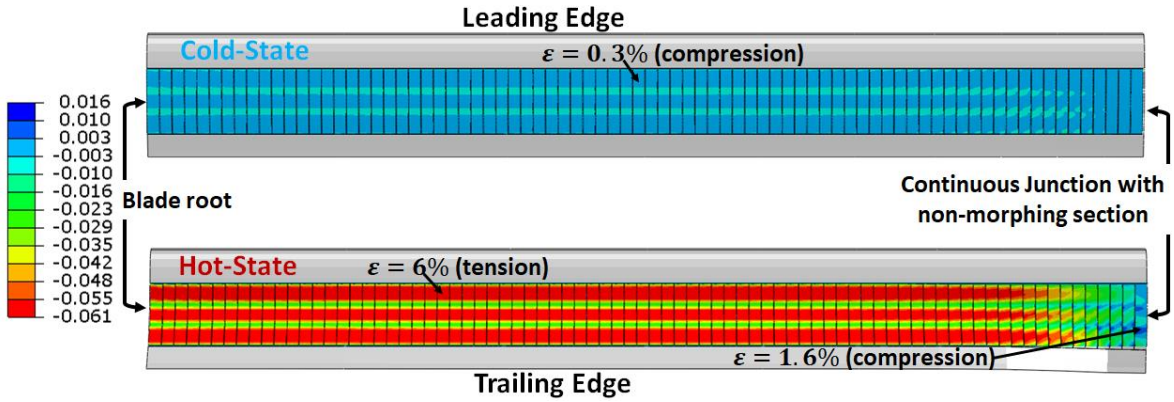

Fig. 28 Chord-wise strain in the SMA strips along the lower blade surface for seamlessly integrated morphing section.

CONCLUSIONS

The current study seeks to advance and improve on the SMA-enabled autonomous camber morphing rotor blade concept developed in Ref. 22. Specific advancements include the use of trained SMA that present a TWSME that in turn results in significantly reducing or eliminating high SMA pre-stress requirements and high strains in the blade to achieve adequate deformation.

First, the minimum number of intermediate spars to support the SMA skin is determined such that maximum camber deformation is achieved while ensuring enough support by the intermediate spars to the SMA skin to prevent local out-of-plane deformation under aerodynamic pressure load. Results suggest that a design with two intermediate spars achieves maximum camber deformation while providing enough support to the SMA skin to resist local deformation under aerodynamic load.

Next, two sets of analysis are carried out for a morphing

blade section that extends 50% inboard of the prismatic derivative of the UH-60A Black Hawk helicopter blade while considering two type of boundary condition between the morphing and non-morphing section (slit and continuous). In both cases, change in ambient temperature between 40-170^{o}F yields camber deformation, expressed as an equivalent flap angle, of 11.5^{o}.

In the case of an applied continuous boundary condition between the morphed and immobile sections, large gradient in camber deformation is observed close to the junction with the non-morphing section. This induces large stress concentrations around the trailing edge section, close to the junction with the non-morphing part of the blade. Several design options are available to alleviate the large strains, such as: (i) modify the properties of the SMA strips near the junction resulting in reduced deformation of the strips for the same increase in ambient temperature; (ii) increase the gap between the SMA strips near the junction which results in reduced force applied by the SMA strips to the morphing section; and (iii) tailor the cross-sectional stiffness of the morphing section near the junction to achieve smaller camber gradient near the junction to the non-morphing section.

Finally, eliminating the need to provide a pre-strain to the baseline configuration significantly reduces the maximum strain and stress in the upper (conformable/passive) skin and the rest of the morphing blade section.

Author contact:
Etana Ferede: ferede@rpi.edu
Anargyros Karakalas: karakalas@tamu.edu
Farhan Gandhi: fgandhi@rpi.edu
Dimitris Lagoudas: lagoudas@tamu.edu

REFERENCES

1. G. Apuleo, “Aircraft Morphing-An Industry Vision,” Morphing Wing Technologies: Large Commercial Aircraft and Civil Helicopters, 2018.
2. P. Della Vecchia, S. Corcione, R. Pecora, F. Nicolosi, I. Dimino and A. Concilio, “Design and integration sensitivity of a morphing trailing edge on a reference airfoil: The effect on high-altitude long-endurance aircraft performance,” Journal of Intelligent Material Systems and Structures, vol. 28, no. 20, 2017.
3. S. A. Snow and D. F. Hunsaker, “Design and performance of a 3D-printed morphing aircraft,” AIAA Scitech 2021 Forum, 2021.
4. I. Dimino, G. Andreutti, F. Moens, F. Fonte, R. Pecora and A. Concilio, "Integrated design of a morphing winglet for active load control and alleviation of turboprop regional aircraft," Applied Sciences (Switzerland), vol. 11, no. 5, 2021.
5. T. A. Weisshaar, “Morphing aircraft systems: Historical perspectives and future challenges,” Journal of Aircraft, vol. 50, no. 2, 2013.
6. Anusonti-Inthra, P., Sarjeant, R., Frecker, M., and Gandhi, F., “Design of a Conformable Rotor Airfoil Using Distributed Piezoelectric Actuators,” AIAA Journal, Vol. 43, No. 8, Aug. 2005, pp. 1684–1695. doi:10.2514/1.1519.
7. Gandhi, F., Frecker, M., and Nissly, A., “Design Optimization of a Controllable Camber Rotor Airfoil,” AIAA Journal, Vol. 46, No. 1, 2008, pp. 142–153. doi:10.2514/1.24476.
8. Grohmann, B., Maucher, C., and Prunhuber, T.et al., “Multidisciplinary Design and Optimization of Active Trailing Edge for Smart Helicopter Rotor Blade,” Mechanics of Advanced Materials and Structures, Vol. 15, No. 3, 2008, pp. 307–324. doi:10.1080/15376490801907830.
9. Bilgen, O., Kochersberger, K. B., Inman, D. J., and Ohanian, O. J., III, “Macro-Fiber Composite Actuated Simply Supported Thin Airfoils,” Smart Materials and Structures, Vol. 19, No. 5, 2010, Paper 055010. doi:10.1088/0964-1726/19/5/055010.
10. Bilgen,O., Kochersberger,K. B., Inman,D. J., and Ohanian,O. J., “Novel, Bidirectional, Variable Camber Airfoil via Macro-Fiber Composite Actuators,” Journal of Aircraft, Vol. 47, No. 1, 2010, pp. 303–314. doi:10.2514/1.45452.
11. Bernhammer, L.O., Teeuwen, S. P.W., DeBreuker,R., van derVeen, G. J., and van Solingen, E., “Gust Load Alleviation of an Unmanned Aerial Vehicle Wing Using Variable Camber,” Journal of Intelligent Material Systems and Structures, Vol. 25, No. 7, May 2014, pp. 795–805. doi:10.1177/1045389X13511010.
12. Woods, B. K. S., Friswell, M., and Wereley, N., “Advanced Kinematic Tailoring for Morphing Aircraft Actuation,” AIAA Journal, Vol. 52, No. 4, April 2014, pp. 798–788. doi:10.2514/1.J052808.
13. Yokozeki, T., Sugiura, A., and Hirano, Y., “Development of Variable Camber Morphing Airfoil Using Corrugated Structure,” Journal of Aircraft, Vol. 51, No. 3, 2014, pp. 1023–1029. doi:10.2514/1.C032573.
14. Strelec, J. K., Lagoudas, D. C., Khan, M. A., and Yen, J., “Design and Implementation of a Shape Memory Alloy Actuated Reconfigurable Airfoil,” Journal of Intelligent Material Systems and Structures,Vol. 14, Nos. 4–5, 2003, p. 257–273. doi:10.1177/1045389X03034687.
15. Barbarino, S., Pecora, R., Lecce, L., Concilio, A., Ameduri, S., and De Rosa, L., “Airfoil Structural Morphing Based on S.M.A. Actuator Series: Numerical and Experimental Studies,” Journal of Intelligent Material Systems and Structures, Vol. 22, No. 10, July 2011, pp. 987–1004. doi:10.1177/1045389X11416032.
16. Pecora, R., Barbarino, S., Concilio, A., Lecce, L., and Russo, S., “Design and Functional Test of a Morphing High Lift Device for a Regional Aircraft,” Journal of Intelligent Material Systems and Structures, Vol. 22, No. 10, July 2011, pp. 1005–1023. doi:10.1177/1045389X11414083.

17. Ameduri, S., Brindisi, A., Tiseo, B., Concilio, A., and Pecora, R., "Optimization and Integration of Shape Memory Alloy (SMA)-Based Elastic Actuators Within a Morphing Flap Architecture," Journal of Intelligent Material Systems and Structures, Vol. 23, No. 4, March 2012, pp. 381–396. doi:10.1177/1045389X11428672.
18. Bil, C., Massey, K., and Ermira, J. A., "Wing Morphing Control with Shape Memory Alloy Actuators," J. of Intel Material Systems and Structures, Vol. 24, No. 7, May 2013, pp. 879–898. doi:10.1177/1045389X12471866.
19. Prabhakar, T., Gandhi, F., and McLaughlin, D., "A Centrifugal Force Actuated Variable Span Morphing Helicopter Rotor," 63rd Annual AHS Int. Forum and Technology Display, Virginia Beach, VA, May 1-3, 2007.
20. Misiorowski, M., Pontecorvo, M., and Gandhi, F., "A Bi-Stable System for Rotor Span Extension in Rotary-Wing Micro Aerial Vehicles," 23rd AIAA/ASME/AHS Adaptive Structures Conference, AIAA Science and Technology Forum 2015, Jan 5-9, 2015, Kissimmee, Florida
21. Moser, P., Barbarino, S., and Gandhi, F., "Helicopter Rotor Blade Chord Extension Morphing using a Centrifugally Actuated von-Mises Truss," Journal of Aircraft, Vol. 51, No. 5 (2014), pp. 1422-1431. doi: 10.2514/1.C032299.
22. Lake, R. C., Nixon, M. W., Wilbur, M. L., Singleton, J. D., and Mirick, P. H. "A demonstration of passive blade twist control using extension-twist coupling", 33rd Structures, Structural Dynamics and Materials Conference, Structures, Structural Dynamics, and Materials and Co-located Conferences, 1992. doi:10.2514/6.1992-2468.
23. Nampy, S. and Smith, E., "Design Evaluation of Model and Full-scale Flexible Matrix Composites Tiltrotor Blades with Extension-twist Coupling," 62nd AHS Forum, 2006. doi:10.1177/1045389X10369719.
24. Ward, E. A., Chopra, I., and Datta, A., "Design of Self-Twisting Rotor Blades for High-Speed Compound Rotorcraft," 25th AIAA/AHS Adaptive Structures Conference, 2017. doi:10.2514/6.2017-0292.
25. Ward, E. A., Chopra, I., and Datta, A., "RPM Driven Extension-Torsion Coupled Self-Twisting Rotor Blades," AHS International 73rd Annual Forum and Technology Display, 2017.
26. DiPalma, M., Ferede, E., and Gandhi, F., "Optimization of Extension-Twist Coupled Composite Blades for High-Speed Rotorcraft," 74th American Helicopter Society Annual Forum, Phoenix, Arizona, May 15-17, 2018.
27. M. DiPalma and F. Gandhi, "Autonomous camber morphing of a helicopter rotor blade with temperature change using integrated shape memory alloys," *J. Intell. Mater. Syst. Struct.*, 2020, doi: 10.1177/1045389X20953613.
28. D. Lagoudas, D. Hartl, Y. Chemisky, L. Machado, and P. Popov, "Constitutive model for the numerical analysis of phase transformation in polycrystalline shape memory alloys," *Int. J. Plast.*, vol. 32–33, pp. 155–183, 2012, doi: 10.1016/j.ijplas.2011.10.009.
29. D. J. Hartl, A. Solomou, D. C. Lagoudas, and D. Saravanos, "Phenomenological modeling of induced transformation anisotropy in shape memory alloy actuators," *Proc. SPIE 8342, Behav. Mech. Multifunct. Mater. Compos.*, vol. 8342, 2012, doi: 10.1117/12.915972.
30. A. A. Karakalas, T. T. Machairas, A. G. Solomou, and D. A. Saravanos, "Modeling of partial transformation cycles of SMAs with a modified hardening function," *Smart Mater. Struct.*, vol. 28, no. 3, p. 035014, Mar. 2019, doi: 10.1088/1361-665X/aafcd9
31. T. T. Machairas, A. G. Solomou, A. A. Karakalas and D. A. Saravanos, "Effect of shape memory alloy actuator geometric non-linearity and thermomechanical coupling on the response of morphing structures," Journal of Intelligent Material Systems and Structures, vol. 30, no. 14, 2019.